Journal of Catalysis 277 (2011) 54–63

Contents lists available at ScienceDirect

Journal of Catalysis

journal homepage: www.elsevier.com/locate/jcat

Effect of boric oxide doping on the stability and activity of a Cu–SiO_2 catalyst for vapor-phase hydrogenation of dimethyl oxalate to ethylene glycol

Zhe He, Haiqiang Lin, Ping He, Youzhu Yuan *

State Key Laboratory of Physical Chemistry of Solid Surfaces and National Engineering Laboratory for Green Chemical Production of Alcohols–Ethers–Esters, College of Chemistry and Chemical Engineering, Xiamen University, Xiamen 361005, China

ARTICLE INFO

Article history:
Received 13 July 2010
Revised 20 September 2010
Accepted 14 October 2010
Available online 3 December 2010

Keywords:
Silica-supported copper
Boric oxide
Ethylene glycol
Hydrogenation
Stability

ABSTRACT

Stable and efficient B–Cu–SiO_2 catalysts for the hydrogenation of dimethyl oxalate (DMO) to ethylene glycol were prepared through urea-assisted gelation followed by postimpregnation with boric acid. Auger electron spectroscopy and CO adsorption by *in situ* Fourier transform infrared spectroscopy revealed that the Cu^+ species on the catalyst surface increased together with an increase in the amount of boric oxide dopant. X-ray diffraction and N_2O chemisorption indicated that a suitable amount of boric oxide doping tended to improve copper dispersion and retard the growth of copper particles during DMO hydrogenation. Catalytic stability was greatly enhanced in the B–Cu–SiO_2 catalyst with an optimized Cu/B atomic ratio of 6.6, because of the formation and preservation of appropriate distributions of Cu^+ and Cu^0 species on the catalyst surfaces. The effect of boric oxide was attributed to its relatively high affinity for electrons, which tended to lower the reducibility of the Cu^+ species.

1. Introduction

Coal, an alternative to dwindling petroleum, has drawn significant attention in the industrial manufacturing of staple chemicals, such as ethylene glycol (EG), which is widely used in various applications, such as antifreeze, polyester fibers, alkyd resin in polyester manufacture, and solvents [1–3]. In contrast to the production of petroleum-derived EG, the coal-to-EG process mainly consists of three steps: gasification of coal to syngas, catalytic coupling of CO with nitrite esters to dialkyl oxalates such as dimethyl oxalate (DMO), and hydrogenation of oxalates to EG [4–7]. Recently, successful industrialization of the coal-to-EG process in the Tongliao district of northeastern China has become immensely promising, with an annual production scale of 20 million tons. However, there are still numerous technical problems to be solved or strategies that need improvement. One of the most difficult problems is insufficient catalytic activity and stability for vapor-phase hydrogenation of oxalates to EG.

Versatile copper-containing catalysts have long been known to be the most active materials for vapor-phase hydrogenation of oxalates to EG [8–10]. Cupreous active sites are considered to be active for the selective hydrogenation of carbon–oxygen bonds and relatively inactive for the hydrogenolysis of carbon–carbon bonds [8]. Up to now, copper–chromium catalysts have been the preferred industrial catalysts for the coal-to-EG process because they have relatively high catalytic stability and long lifespans [11–15]. Nonetheless, the toxic chromium contained in copper–chromium catalysts is dangerous and inconvenient for practical applications with regard to meeting environmental requirements and ensuring the security of workers. Thus, the development of safe, stable, and active catalysts for the hydrogenation of oxalates to EG has become a challenging endeavor. Among the various reported catalysts active for the hydrogenation of oxalate to EG, silica-supported copper catalysts are outstanding because of the moderate interaction between copper and the silica support, which has relatively weak acidity and is propitious for constructing catalytic centers active for the selective hydrogenation of oxalate to EG [4,16–20].

Various techniques, such as ammonia evaporation, ion exchange, sol–gel, deposition precipitation, and impregnation, have been used to fabricate silica-supported copper catalysts [21,22]. A high initial copper surface area on silica supports was believed to be a key factor in obtaining excellent catalytic activity for the hydrogenation of oxalate to EG. However, silica-supported copper with catalytic activity higher than that of a copper–chromium catalyst has inherent problems, such as poor stability and short lifetime, which severely restricts its industrial application. Generally, catalyst deactivation has been ascribed to two main causes. One is copper coagulation and lost of active cupreous surface, which are usually characterized by a change to a "copper red" color of the deactivated catalyst [23]. Another cause is the valence transition of cupreous species under reaction conditions [22]. The emergence of gray cupric oxalate on deactivated Cu–SiO_2 catalyst strongly implies that the valence of cupreous

* Corresponding author. Fax: +86 592 2183047.
E-mail address: yzyuan@xmu.edu.cn (Y. Yuan).

0021-9517/$ - see front matter © 2010 Elsevier Inc. All rights reserved.
doi:10.1016/j.jcat.2010.10.010

species changes as a result of redox reaction between surface cupreous species and reactants under the conditions of oxalate hydrogenation. Finding a practical way to retain the state of highly dispersed copper has been proposed to be an important strategy to improve the catalytic stability.

Therefore, improvements in average EG yield and extension of the catalyst life cycle are still the major areas of interest for the selective hydrogenation of oxalate to EG [24,25]. A previous report showed that B_2O_3-modified Ni/γ-Al_2O_3 catalysts could possess high metal dispersion and exhibit excellent catalytic stability for steam methane reforming because of the strong interaction between surface nickel and B_2O_3 [26]. However, no study regarding the performance–structure correlation of boron-doped Cu–SiO_2 catalysts in comparison to the boron-free catalyst for the vapor-phase selective hydrogenation of DMO to EG has been published. This study aims to develop catalysts with enhanced catalytic activity and prolonged lifespan for the vapor-phase selective hydrogenation of DMO to EG. A kind of boric oxide-doped Cu–SiO_2 catalyst (B–Cu–SiO_2) prepared by urea-assisted gelation and followed by impregnation with boric acid was first reported. Detailed structural and kinetic studies that address the effects of the boric oxide were then shown.

2. Experimental

2.1. Catalyst preparation

A Cu–SiO_2 catalyst with a preset copper loading of 30 wt% was prepared by urea-assisted gelation [27,28]. Briefly, 10.5 g of 40 wt% Ludox as 40 colloidal silica was dispersed in 100 ml of aqueous solution containing 3.0 g of urea, 11.7 g 28 wt% aqueous ammonia, and 6.8 g of $Cu(NO_3)_2{\cdot}3H_2O$ in a round-bottomed flask. The suspension was vigorously stirred at 353 K in an oil bath for 4 h. The light blue precipitate obtained was separated by hot filtration, washed thrice with deionized water, and dried overnight under vacuum at 393 K to yield an azure powder of Cu–SiO_2 precursors. Boric oxide-modified Cu–SiO_2 catalyst precursors were prepared by an impregnation method. First, an aqueous solution of H_3BO_3 was dropped onto the Cu–SiO_2 precursor in a 100-ml beaker. The slurry was aged for 2 h at room temperature, dried overnight at 393 K, and then calcined for 2 h at 623 K in air, yielding boric oxide-modified Cu–SiO_2 catalyst precursors. The precursors were denoted as *x*B–Cu–SiO_2, where *x* stands for the preset mass loading of boron.

2.2. Catalyst characterization

The wide-angle normal and *in situ* X-ray diffraction (XRD) measurements of the samples were performed on a Panalytical X'pert Pro Super X-ray diffractometer using Cu Kα radiation (λ = 0.15418 nm) with a scanning angle (2θ) ranging from 10° to 90°. The tube voltage was 40 kV and the current was 30 mA. The full width at half maximum (FWHM) of Cu (1 1 1) diffraction at a 2θ of 43.2° was used to calculate the Cu crystallite size using the Scherrer equation. For *in situ* XRD measurement, a catalyst precursor was placed in a stainless steel holder and covered with a beryllium plate having a thickness of 0.1 mm. Then a 5% H_2–95% Ar mixture was introduced at a flow rate of 50 cm^3 min^{-1}. Temperature ramping programs were performed from room temperature to 473, 523, 573, 623, 673, 723, 773, 873, 973, 1073, and 1173 K at a rate of 5 K min^{-1}. The XRD patterns were collected after samples reached the preset temperatures for 30 min. The diffraction pattern was identified by matching them with reference patterns included in the JCPDS data base.

Nitrogen adsorption–desorption isotherms were measured by static N_2 physisorption at 77 K with a Micromeritics TriStar II 3020 surface area and pore analyzer. Before the N_2 physisorption measurement, all samples were outgassed at 393 K for 1 h and then evacuated at 573 K for 3 h to remove physically adsorbed impurities. The specific surface area (S_{BET}) was calculated by the Brunauer–Emmett–Teller (BET) method. The total pore volume (V_p) was derived from the adsorbed N_2 volume at a relative pressure of approximately 0.99, and the Barrett–Joyner–Halenda (BJH) method was used to calculate the pore size distributions according to the desorption branch of the isotherms.

The reducibility of the calcined sample was determined by H_2 temperature-programmed reduction (TPR) on a Micromeritics Autochem II 2920 instrument connected to a Hiden Qic-20 mass spectrometer (MS). Prior to the TPR test, the catalyst was pretreated in a quartz U-tube reactor at 523 K for 1 h under a gas flow of 20% O_2–80% Ar at a rate of 50 cm^3 min^{-1} to drive off physically adsorbed impurities. After the catalyst cooled to room temperature under argon, 5% H_2–95% Ar was introduced at a flow rate of 50 cm^3 min^{-1}, and then the temperature was ramped linearly from ambient temperature to 1073 K at a rate of 10 K min^{-1}. Hydrogen consumption was simultaneously monitored by a thermal conductivity detector (TCD) and MS.

The catalysts were also analyzed by CO_2 and NH_3 temperature-programmed desorption (TPD) on a Micromeritics Autochem II 2920 instrument connected to a Hiden Qic-20 MS. For basicity evaluation by CO_2-TPD, 100 mg of the catalyst sample in a quartz U tube was first reduced in 5% H_2–95% Ar at 623 K for 4 h, and then the gas was switched to CO_2, which passed through the catalyst bed for 1 h at 373 K. Weakly adsorbed CO_2 was removed by pure argon sweeping at room temperature until the baseline of TCD and MS signals stabilized. Under an atmosphere of pure argon with a rate of 50 cm^3 min^{-1}, CO_2-TPD was conducted from room temperature to 873 K at a heating rate of 5 K min^{-1}. The desorbed CO_2 was monitored with a MS signal of m/e = 44 in multiple ion detection (MID) mode. For acidity evaluation by NH_3-TPD, 100 mg of Cu–SiO_2 sample was first reduced in 5% H_2–95% Ar at 623 K for 4 h and then cooled to ambient temperature. Then a 10% NH_3–90% Ar stream was introduced to sweep through the catalyst bed for 30 min at 373 K. Weakly adsorbed NH_3 was removed by pure argon sweeping at 373 K until the baseline of TCD and MS signals stabilized. Under an atmosphere of purified Ar with a flow rate of 50 cm^3 min^{-1}, NH_3–TPD was conducted from room temperature to 1073 K with a ramping rate of 5 K min^{-1}. Desorbed NH_3 was monitored with an MS signal of m/e = 16 and 17 in MID mode, and desorbed H_2O was also inspected at an MS signal of m/e = 18.

Transmission electron microscopy (TEM) micrographs were obtained on a Tecnai F30 apparatus operated at 300 kV. The catalyst samples were ultrasonically dispersed in ethanol at room temperature for 30 min. The as-obtained solution was dropped onto the copper grid for TEM.

The dispersion and metallic copper surface areas of the catalysts were determined by N_2O chemisorption at 333 K using a procedure described in the literature [28]. Briefly, 100 mg of Cu–SiO_2 calcined at 623 K was reduced in 5% H_2–95% Ar at 623 K for 4 h and cooled to 333 K. Then pure N_2O was introduced at a rate of 30 cm^3 min^{-1} for 1 h, ensuring that surface Cu atoms were completely oxidized according to the reaction $2Cu_{(s)} + N_2O \rightarrow Cu_2O_{(s)} + N_2$. The quantity of irreversibly chemisorbed O_2 atoms was measured by a hydrogen pulse chromatographic technique on a Micromeritics Autochem II 2920 equipped with a TCD. Hydrogen pulse reduction of surface Cu_2O to metallic copper was conducted at 573 K to ensure that the chemisorbed oxygen on the copper surface immediately reacted with pure hydrogen gas introduced from the pulse loop to form water, and the formed water was soon removed by a 13× dehydration tube in the reaction outlet. Hydrogen pulse-dosing was repeated until the pulse area no longer changed. The consumed amount of hydrogen was the value obtained by subtracting

the small area of the first few pulses from the area of the other pulses. Copper loading of all reduced catalysts was analyzed by inductively coupled plasma optical emission spectrometry (ICP-OES) on a Thermo Electron IRIS Intrepid II XSP. Copper dispersion was calculated by dividing the amount of chemisorption sites into total supported copper atoms.

The infrared (IR) spectra were recorded on a Nicolet 6700 spectrometer with a spectral resolution of 4 cm^{-1}. The self-supporting wafer prepared from the pure catalyst powder was placed in a lab-made *in situ* IR cell, together with a high-vacuum turbo pump with a residual pressure below 10^5 Pa. All samples were reduced under an H_2 flow at 623 K for 4 h in the cell. The cell was then evacuated for 30 min to remove the chemisorbed hydrogen species. Afterward, the sample was cooled to room temperature and pure CO (10^5 Pa) was admitted into the cell for 30 min. The spectra were then collected at different evacuation times and temperatures.

X-ray photoelectron spectroscopy (XPS) and Auger electron spectroscopy (XAES) were carried out on a Quantum 2000 Scanning ESCA Microprob instrument (Physical Electronics) equipped with an Al Kα X-ray radiation source ($h\nu$ = 1486.6 eV). To obtain the surface states of catalysts under the reaction conditions, the samples were collected by the following procedure. The catalyst samples were pressed into thin disks, placed in a reactor, and reduced in a flow of 5% H_2–95% Ar at 623 K for 6 h. Then the DMO hydrogenation under conditions of 463 K, 3.0 MPa, H_2/DMO = 80, and weight liquid hourly space velocity ($WLHSV_{DMO}$) of 0.75 $g_{\text{-DMO}}\ g^{-1}_{\text{-catal}}\ h^{-1}$ (for short h^{-1}) was carried out over the catalysts for 46 h to reach a steady state. After that, the supply of DMO substrate and hydrogen was stopped and a purified Ar stream was introduced into the catalyst bed. When the catalyst was cooled to room temperature, the reactor containing the catalyst samples was carefully sealed under Ar. The samples were then placed on holders in a glove box under Ar, outgassed to less than 2.6×10^5 Pa in a prechamber, and transferred to an analysis chamber. The binding energies were calibrated using the Si2I peak at 103.7 eV as the reference. The experimental errors were within ±0.2 eV.

2.3. Measurement of catalytic activity

The DMO hydrogenation reaction was conducted in continuous flow mode in a stainless steel tubular reactor equipped with a computer-controlled autosampling system. Typically, 500 mg of catalyst precursor (4060 meshes) was loaded into the center of the reactor and both sides of the catalyst bed were packed with quartz powders (4060 meshes). Before catalytic performance was evaluated, all catalyst precursors were prereduced in 5% H_2–95% Ar atmosphere at 623 K for 4 h with a ramping rate of 2 K min^{-1}. Then the catalyst bed was cooled to 443473 K. Pure H_2 was fed into the reactor, and the system pressure was held at 3.0 MPa with the aid of a back-pressure regulator. A 3 wt% DMO methanol solution was pumped into the catalyst bed with a Series III digital HPLC pump (Scientific Systems, Inc.). The products were analyzed with a Shimadzu GC-2010 gas chromatograph (GC) fitted with a DB-FFAP capillary column (30 m × 0.45 mm × 0.85 μm) and a flame ionization detector with relative standard deviation (RSD) less than 2%. Under a given condition, the kinetic data were collected by six samplings at an interval of 30 min after the reaction attained a steady state. The RSD of analysis data for each sampling was less than 3%.

Heat treatment at higher temperatures was performed to investigate the thermal resistance of Cu–SiO_2 and B–Cu–SiO_2 catalysts. Typically, the steady space time EG yield for the freshly reduced catalyst, labeled as STY_F, was first measured at 483 K and a DMO WLHSV of 3.5 h^{-1}. Then the reaction temperature was raised to 623 K and the DMO hydrogenation was held under this severe condition for 24 h. After that, the space time EG yield of the catalyst after heat treatment, labeled as STY_T, was evaluated at 483 K and the same $WLHSV_{DMO}$ of 3.5 h^{-1}. The ratio STY_T:STY_F was used to estimate and compare the stability of different catalysts.

3. Results

3.1. Catalytic activity and stability

Vapor-phase DMO hydrogenation is known to comprise several continuous reactions, including DMO hydrogenation to methyl glycolate (MG), MG hydrogenation to EG, and deep hydrogenation of EG to ethanol. Moreover, byproducts of 1,2-butanediol (1,2-BDO) and 1,2-propanediol (1,2-PDO) are also produced as a result of the dehydration reaction between EG and ethanol or methanol [27,28]. The catalytic performance of Cu–SiO_2 and B–Cu–SiO_2 catalysts for vapor-phase DMO hydrogenation to EG is listed in Table 1. At a high DMO WLHSV of 6.0 h^{-1}, the Cu–SiO_2 catalyst

Table 1
Comparison of vapor-phase hydrogenation of DMO to EG over Cu–SiO_2 and B–Cu–SiO_2 catalysts.[a]

Catalysts	$WLHSV_{(DMO)}$ (h^{-1})	$STY_{(EG)}$ (h^{-1})[b]	Conversion (%)	Selectivity (%)			
				EG	MG	EtOH	1,2-PDO + BDO[c]
Cu–SiO_2	6.0	0.39	46.8	26.2	73.7	0.0	0.7
	0.75	0.35	99.6	88.6	4.9	2.9	3.6
0.5B–Cu–SiO_2	6.0	0.55	53.1	32.7	66.6	0.0	0.8
	0.75	0.36	99.6	91.5	3.5	3.0	2.1
1B–Cu–SiO_2	6.0	0.77	61.9	39.4	59.8	0.0	0.8
	0.75	0.37	99.7	93.0	3.3	1.8	1.9
3B–Cu–SiO_2	6.0	0.38	46.0	26.4	72.8	0.0	0.8
	0.75	0.35	99.8	89.2	5.4	4.0	1.4
5B–Cu–SiO_2	6.0	0.34	44.4	24.3	74.7	0.0	1.0
	0.75	0.34	99.8	87.2	5.2	7.1	0.5
7B–Cu–SiO_2	6.0	0.26	37.5	21.8	77.4	0.0	0.8
	0.75	0.34	99.2	86.7	5.8	7.0	0.4
10B–Cu–SiO_2	6.0	0.16	26.3	19.7	79.5	0.0	0.8
	0.75	0.33	99.3	83.3	6.3	5.0	0.1

[a] Reaction conditions: T = 463 K, $P(H_2)$ = 3.0 MPa, H_2/DMO = 80.
[b] STY represents the space time yield of EG for the fresh catalysts, grams of product per gram of catalyst per hour ($g\ g^{-1}_{\text{-catal}}\ h^{-1}$, for short h^{-1}).
[c] Sum of byproducts 1,2-PDO and 1,2-BDO.

exhibited a DMO conversion of 46.8% and a relatively low selectivity of 26.2% to EG. Doping boric oxide in Cu–SiO_2 catalyst with a boron loading in the range of 0.510 wt% significantly changed the catalytic performance, showing volcano-type catalytic behavior in terms of conversion and EG selectivity. Among the catalysts, 1B–Cu–SiO_2 with a Cu:B atomic ratio of 6.6 afforded the highest DMO conversion of 61.9% and EG selectivity of 39.4%. At a low DMO WLHSV of 0.75 h^{-1}, the conversion was >99% for all catalysts, while the best EG selectivity of 93.0% was obtained on the 1B–Cu–SiO_2 catalyst. The results implied that moderately tuning boric oxide coverage on the surface of Cu–SiO_2 and the interaction between cupreous species and boric oxide could be of importance for optimizing the catalytic performance. Moreover, in the case of lower DMO WLHSV, side reactions of deep hydrogenation and dehydration became relatively intense. The selectivity for ethanol byproduct increased, whereas that for 1,2-BDO and 1,2-PDO decreased with the increase of boron loading. Variations of the strength and quantity of acidic and basic sites on the B–Cu–SiO_2 catalyst, induced by acidic boric oxide modification for different doping amounts, were presumed to be responsible for the change in byproduct distribution. Acidic sites are beneficial to deep hydrogenation of EG to ethanol, whereas basic sites are helpful for the dehydration between EG and ethanol, or methanol, into 1,2-BDO, and 1,2-PDO [29,30].

The long-term stability and activity of catalysts are vital for vapor-phase DMO hydrogenation to EG from both academic and industrial viewpoints. A comparison of catalytic activity as a function of reaction time for 1B Cu SiO_2 and Cu SiO_2 catalysts is displayed in Fig. 1. The 1B–Cu–SiO_2 catalyst showed excellent catalytic performance at 463 K, which was stable for 300 h. In contrast, obvious deactivation of boron-free Cu–SiO_2 was observed within 30 h under identical reaction conditions. An evaluation of the stability of B–Cu–SiO_2 and Cu–SiO_2 catalysts was also conducted following a kind of thermal-resistance test (Table 2), which is usually adopted for copper catalysts for the transformation of syngas to methanol. The catalytic performance for B–Cu–SiO_2 and Cu–SiO_2 catalysts after thermal treatment at 623 K for 24 h was significantly different. For 0.5B–Cu–SiO_2 and 1B–Cu–SiO_2 catalysts with relatively low boric oxide doping amounts, the thermal stability was notably enhanced over that of Cu–SiO_2. The STY_T:STY_F ratios for the 0.5B–Cu–SiO_2 and 1B–Cu–SiO_2 catalysts were 0.75 and 0.76, respectively, but that for Cu–SiO_2 was only 0.66. Nevertheless, a further increase in boric oxide doping amount lowers the thermal stability because the STY_T/STY_F ratios for 3B–Cu–SiO_2, 5B–Cu–SiO_2, 7B–Cu–SiO_2, and 10B–Cu–SiO_2 considerably dwindled with the increase of boric oxide doping.

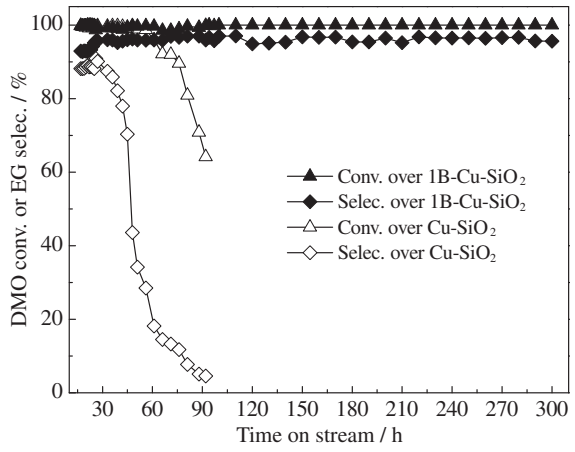

Fig. 1. Catalytic performance of Cu–SiO_2 and 1B–Cu–SiO_2 as a function of reaction time. The reaction conditions are the same as in Table 1.

Table 2
Catalytic properties of Cu–SiO_2 and B–Cu–SiO_2 catalysts before and after heat treatment.[a]

Catalysts	Cu/B atomic ratio[b]	STY_F (h^{-1})[c]	STY_T (h^{-1})[d]	Ratio of STY_T/STY_F
Cu–SiO_2	∞	1.6	1.1	0.66
0.5B–Cu–SiO_2	11.3	1.6	1.2	0.75
1B–Cu–SiO_2	6.6	1.6	1.3	0.76
3B–Cu–SiO_2	1.5	1.6	1.0	0.63
5B–Cu–SiO_2	1.4	1.6	0.8	0.51
7B–Cu–SiO_2	0.7	1.6	0.5	0.32
10B–Cu–SiO_2	0.6	1.6	0.4	0.27

[a] Reaction conditions: T = 483 K, $WLHSV_{(DMO)}$ = 3.5 h^{-1}, $P(H_2)$ = 3.0 MPa, H_2/DMO = 80.
[b] Calculated with the data determined by ICP-AES.
[c] STY_F represents the space time yield of EG for the fresh catalysts, grams of product per gram of catalyst per hour (g g^{-1}_{-catal} h^{-1}, for short h^{-1}). Data were collected after time on stream of 4 h.
[d] STY_T represents the space time yield of EG for the catalysts after heat treatment at 623 K for 24 h, grams of product per gram of catalyst per hour (g g^{-1}_{-catal} h^{-1}, for short h^{-1}). Data were collected after time on stream of 4 h.

3.2. Characterization of the catalysts

3.2.1. Physicochemical properties of the catalysts

Table 3 lists the chemical compositions and textural properties of Cu–SiO_2 and B–Cu–SiO_2 with different boron doping amounts. The actual copper loading was slightly lower than the preset value of the designed composition for urea-assisted gelation because cupric ions weakly absorbed on silica gel were eluted during the centrifugal washing process of the catalyst precursor, while the boron doping amount for B–Cu–SiO_2 was close to the preset values determined by ICP-OES. The N_2 adsorption–desorption isotherms of reduced Cu–SiO_2 and B–Cu–SiO_2 samples indicated that all samples exhibited Langmuir type IV isotherms with H1-type hysteresis loops (Fig. S1 in the Supplementary Material) [31–33]. The Cu–SiO_2 sample prepared by urea-assisted gelation was found to possess a relatively high BET surface area of 379.4 m^2 g^{-1} and a pore volume of 1.0 cm^3 g^{-1} (Table S1 in the Supplementary Material). It was a kind of mesoporous material with an average pore diameter of 10.1 nm, analogous to a traditional silica sphere synthesized by sol–gel. Boric oxide doping with a boron loading no higher than 1 wt% slightly influenced the specific surface area, pore volume, and average pore diameter, whereas further increasing boron loading in the range of 110 wt% resulted in a gradual decline in both surface area and pore volume. Boric oxide, which has a low melting point of 773 K and was introduced by impregnation, was assumed to tend to cover the Cu–SiO_2 surface and plug channels or pores, resulting in a decrease of internal surface areas and accessible pore volumes.

Metallic surface-to-volume ratios and concentrations of cupreous surface have been viewed as significantly affecting the physicochemical properties and catalytic performance of copper-based catalysts [34]. The metallic copper dispersions and cupreous surface areas of Cu–SiO_2 and B–Cu–SiO_2 catalysts were determined by a frequently used technique of dissociative N_2O chemisorptions on surface copper atoms (Table 3). Although boron doping in the range of 0.51 wt% (actual boron loading of 0.40.7 wt%) did not notably change the specific surface area and pore volume, it brought about nonnegligible enhancement of copper dispersion. A similar promoting effect on boron modified Ni catalyst has also been reported by Chen et al. [35]. Notably, the highest copper dispersion (0.24) was obtained on 1B–Cu–SiO_2, which afforded the highest EG yield (Table 1). The promoting effect on copper dispersion might be ascribed to the fact that boric oxide acted as a kind of isolating agent to inhibit thermal transmigration and accumulation of copper nanoparticles during the processes of hydrogen

Table 3
Structural properties and chemical compositions of Cu–SiO_2 and B–Cu–SiO_2 catalysts.

Catalysts	Cu loading (wt%)[a]	B loading (wt%)[a]	S_{BET} ($m^2\ g^{-1}$)[b]	Cu dispersion (%)[c]	SA_{Cu} ($m^2\ g^{-1}$)[c]
Cu–SiO_2	26.2	0	379.4	18.2	31.0
0.5B–Cu–SiO_2	26.6	0.4	383.1	21.3	36.8
1B–Cu–SiO_2	27.0	0.7	383.4	24.4	42.8
3B–Cu–SiO_2	27.7	3.1	345.2	15.8	28.5
5B–Cu–SiO_2	28.9	3.6	336.3	10.8	20.4
7B–Cu–SiO_2	27.1	6.7	238.8	10.3	18.1
10B–Cu–SiO_2	29.4	9.0	218.1	4.0	7.0

[a] Determined by ICP-OES.
[b] BET specific surface area.
[c] Determined by N_2O surface oxidation; SA: Cu metallic surface area.

reduction and DMO hydrogenation. However, boric oxide doping with a boron loading above 3 wt% reduced, instead of increased, copper dispersion on B–Cu–SiO_2. It was speculated that most copper crystallites were covered by films of boric oxide on the catalyst surface and became inaccessible for N_2O molecules when boric oxide concentration was increased. On the other hand, the strong interaction between acidic boric oxide and cupreous species was also considered to play an important role in altering the physicochemical properties of Cu–SiO_2 catalysts.

3.2.2. Evolution of crystalline phase and morphology

The XRD pattern of the Cu–SiO_2 catalyst calcined at 623 K exhibited a nearly amorphous state (Fig. S2 in the Supplementary Material). Extremely weak and broad diffraction peaks at 2θ of 31.0°, 34.8°, 57.2°, 63.3°, and 71.2° were assigned to the copper phyllosilicate phase (JCPDS 00-003-0219) [36]. No diffraction peaks for cupric oxide or any related cupreous substances could be observed, indicating that copper was highly dispersed in the porous silica support. Introduction of boric oxide onto Cu–SiO_2 catalyst precursors did not significantly change the XRD patterns of Cu–SiO_2 catalyst precursors, but diffraction peaks at 2θ of 15.0° and 27.8° for boric oxide (JCPDS 06-0297) gradually emerged when the doping amount of boron was higher than 6 wt% in the B–Cu–SiO_2 catalyst.

Highly dispersed metallic copper exposed to the atmosphere tended to be oxidized to different extents depending on exposure time and temperature. Thus, *in situ* XRD characterization was adopted to monitor the phase evolution of Cu–SiO_2 and B–Cu–SiO_2 catalysts under 5% H_2–95% Ar as a function of reduction temperature (Fig. S3 in the Supplementary Material). A diffraction peak at 2θ of 43.2°, characteristic of Cu (1 1 1) (JCPDS 04–0836), became observable because some Cu^{2+} species on the Cu–SiO_2 catalyst precursor were reduced to Cu^0 when the reduction temperature was ramped to 523 K. The Cu (1 1 1) diffraction peak observed at a reduction temperature lower than 973 K was broad, and no obvious diffraction peaks of other crystal faces could be observed, strongly indicating that nascent crystalline copper was highly dispersed on the Cu–SiO_2 catalyst. Further increasing the reduction temperature inevitably caused the accumulation and coagulation of metallic copper, as evidenced by the gradual sharpening of copper diffraction peaks. The copper crystallite size calculated by the Scherrer equation significantly grew from 3.9 to 14.8 nm when the reduction temperature increased from 523 to 1173 K. The phase evolution of the 1B–Cu–SiO_2 catalyst precursor under 5% H_2–95% Ar as a function of reduction temperature showed no obvious difference from the Cu–SiO_2 catalyst (Fig. S3 in the Supplementary Material).

The XRD patterns of the working catalysts Cu–SiO_2 and B–Cu–SiO_2 after heat treatment at 623 K are shown in Fig. 2. To avoid and diminish phase transformation that probably occurred during exposure to an oxidative atmosphere, catalysts were carefully collected under hydrogen at room temperature and sealed in glass bottles until XRD analysis. After thermal treatment, peaks for metallic copper grew stronger to different degrees, and the characteristic diffraction peaks of Cu_2O (JCPDS 034-1354) at 2θ of 36.6°, 42.4°, and 61.5° appeared for Cu–SiO_2 and B–Cu–SiO_2 with different intensities. For B–Cu–SiO_2 catalysts with relatively low boron loadings in the range of 0.40.7 wt%, the copper diffraction intensity increased less significantly than that of Cu–SiO_2 without boric oxide modification. The results clearly demonstrated that a suitable amount of boric oxide dopant in the catalyst was helpful for retarding the growth of metallic copper crystallites. However, the intensity of the metallic copper diffraction peak and the copper crystallite size calculated by the Scherrer equation increased with an increase in boron loading when the loading was higher than 3 wt%. On the other hand, the boric oxide amount also affected the diffraction intensity of Cu_2O after thermal treatment. The Cu_2O(1 1 1) peaks at a 2θ of 36.6° on 0.5B–Cu–SiO_2, 1B–Cu–SiO_2, and 3B–Cu–SiO_2 were slightly more intense than that of Cu–SiO_2, but those on high-boron-loading catalysts, such as 5B–Cu–SiO_2, 7B–Cu–SiO_2, and 10B–Cu–SiO_2, became weaker. Since no Cu_2O phase was observed during hydrogen reduction, as confirmed by *in situ* XRD (Fig. S3 in the Supplementary Material), the formation of Cu_2O might be the product of redox between copper crystallites and reaction substrates or products, such as DMO, MG, or EG, during DMO hydrogenation. The results implied that the variation of interactions among cupreous species, boric oxide, and the silica support significantly altered the stability and redox property of copper crystallites, in accordance with the boric oxide loadings.

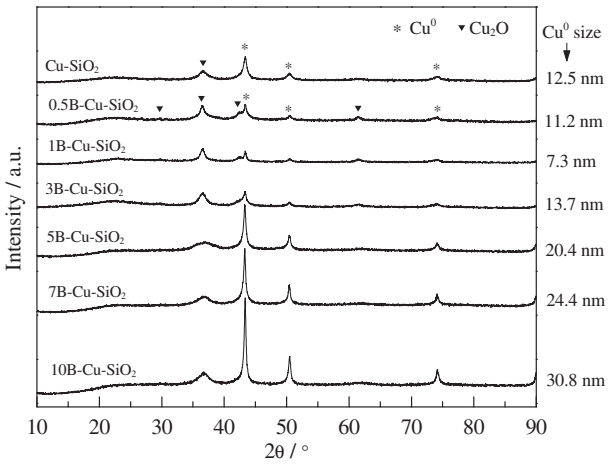

Fig. 2. XRD patterns of Cu–SiO_2 and *x*B–Cu–SiO_2 catalysts after heat treatment at 623 K for 24 h.

TEM images for the as-reduced Cu–SiO_2 and 1B–Cu–SiO_2 samples indicated that most of the copper crystallites had particle sizes smaller than 5 nm and were well-dispersed in the SiO_2 matrix,

although the copper loading was as high as 30 wt% (Fig. S4 in the Supplementary Material). The particle sizes were in good agreement with those estimated by the Scherrer equation. However, it was not easy to observe the Cu particles with regular shape in both samples, even though the magnification of the TEM image was increased to 8×10^5.

3.2.3. Reducibility and surface acid–base properties

TPR characterizations were performed to investigate the reducibility of Cu–SiO_2 and B–Cu–SiO_2 samples calcined at 623 K (Fig. 3). The boric oxide-free Cu–SiO_2 sample displayed a sharp reduction peak centered at 528 K, while the B–Cu–SiO_2 with boric oxide modification showed a higher reduction temperature and the temperature was gradually increased with increased boron amount. Highly dispersed cupreous species on silica supports have been well documented to be more readily reduced than bulk cupric oxide, and the typical reduction temperature is around 530 K [23]. Accordingly, the low reduction temperature of 528 K for Cu–SiO_2 strongly suggested that urea-assisted gelation could be adopted to finely disperse cupreous species on silica support at a high copper loading (~30 wt%). This is in agreement with the results deduced from XRD and TEM measurements. The tendency of boric oxide doping to raise the reduction temperature was probably due to the chemical interaction between the acidic boric oxide and the basic cupric oxide. When the boric oxide amount increased and the Cu/B molar ratio decreased, gaining electrons during hydrogen reduction became harder for the cupreous species because the electron affinity of boric oxide was higher than that of SiO_2. A shoulder peak that appears in addition to the main reduction peak for 3B–Cu–SiO_2 and 5B–Cu–SiO_2 may result from new cupreous species, such as cupric borate formed on Cu–SiO_2 by boric acid impregnation and calcination at 623 K.

The NH_3-TPD and CO_2-TPD measurements were carried out to evaluate the strength and quantity of acidic and basic sites on Cu–SiO_2 and B–Cu–SiO_2 catalysts and the obtained profiles are shown in Figs. 4 and 5, respectively. No obvious desorption peak of NH_3 could be observed, whereas CO_2 desorption occurred in a relatively high temperature range of 535890 K for the Cu–SiO_2 catalyst reduced at 623 K, indicating that moderate to strong basic sites dominated the Cu–SiO_2 surface. Acidic sites with an NH_3 desorption peak at 442 K gradually grew stronger with an increase in boron loading, suggesting that boric oxide was responsible for the acidity and its amount determined the quantities of surface acidic sites. On the other hand, boric oxide doping affected not only the quantity but also the strength of basicities on the Cu–SiO_2 surface. For the 0.5B–Cu–SiO_2 catalyst, boric oxide doping resulted in the disappearance of most of the strongest basic sites with a CO_2 desorption peak at 736 K and the appearance of weak basic sites with a CO_2 desorption peak at 368 K. Moderately basic sites with a CO_2 desorption peak at 590 K did not exhibit significant changes. Further increasing the boric oxide doping amount tended to weaken and then eliminate basic sites with the desorption peak at 590 K. Notably, variation of the boron doping amount in the range of 0.510 wt% did not significantly change the shape and intensity of CO_2 desorption peak at 368 K. Therefore, the transformation of the acidities and basicities induced by boric oxide doping could be explained by the neutralization that occurred between the acidic boric oxide and the basic sites on the Cu–SiO_2 surface. However, further studies are still in progress to gain insight into the structurally related surface acidic and basic sites.

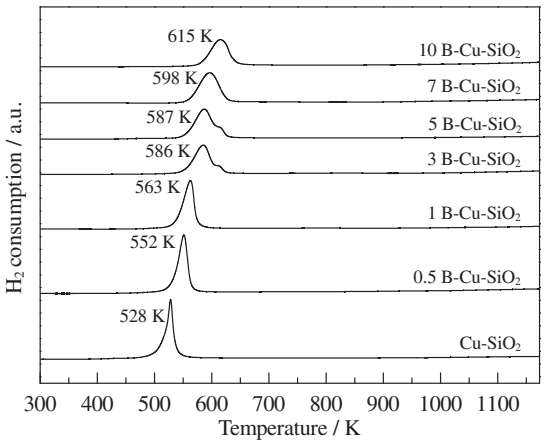

Fig. 3. TPR profiles of Cu–SiO_2 and *x*B–Cu–SiO_2 catalyst precursors.

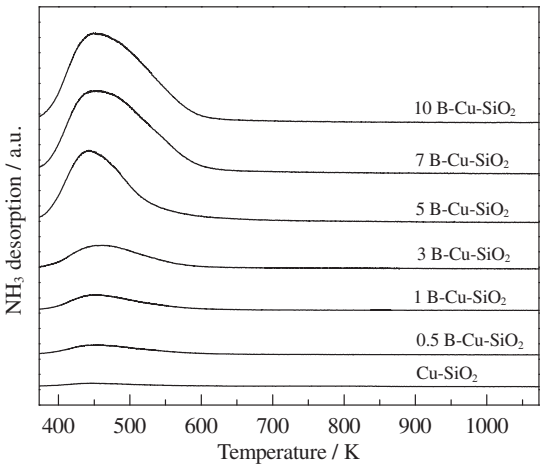

Fig. 4. NH_3-TPD profiles of Cu–SiO_2 and *x*B–Cu–SiO_2 catalysts.

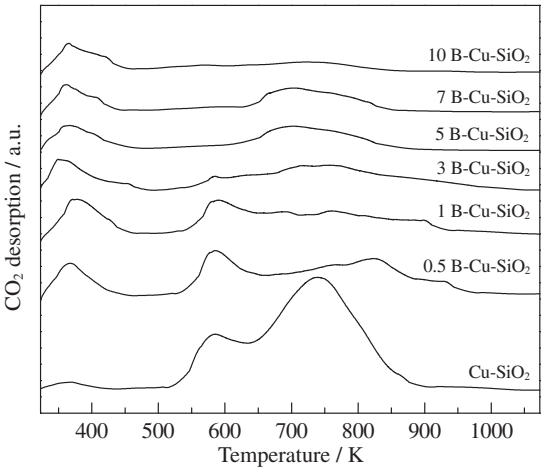

Fig. 5. CO_2-TPD profiles of Cu–SiO_2 and *x*B–Cu–SiO_2 catalysts.

3.2.4. Surface chemical states and the role of boron

The XPS and XAES spectra of working catalysts of Cu–SiO_2 and B–Cu–SiO_2 are illustrated in Figs. 6 and 7, respectively. For comparison, the XPS and XAES spectra of as-reduced samples of Cu–SiO_2 and B–Cu–SiO_2 are displayed in Figs. S5 and S6 in the Supplementary Material, respectively. Typically, the Cu2*p*3/2 binding energy of CuO is found at around 933.5 eV, and the binding energy for well-dispersed Cu^{2+} species strongly interacting with silica supports is detected at above 934.9 eV [23,37]. Only the Cu2$p_{3/2}$ and Cu2$p_{1/2}$ peaks centered at binding energies of 932.7 and 952.5 eV, conventionally assigned to Cu^+ or Cu^0 species, were

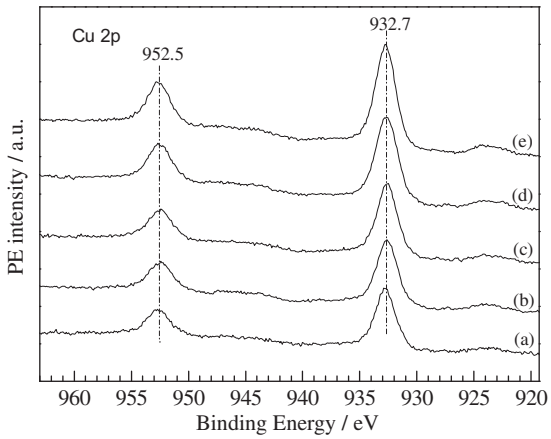

Fig. 6. Cu2*p* XPS spectra of Cu–SiO_2 and B–Cu–SiO_2 catalysts after DMO hydrogenation for 6 h: (a) Cu–SiO_2, (b) 0.5B–Cu–SiO_2, (c) 1B–Cu–SiO_2, (d) 3B–Cu–SiO_2, (e) 5B–Cu–SiO_2.

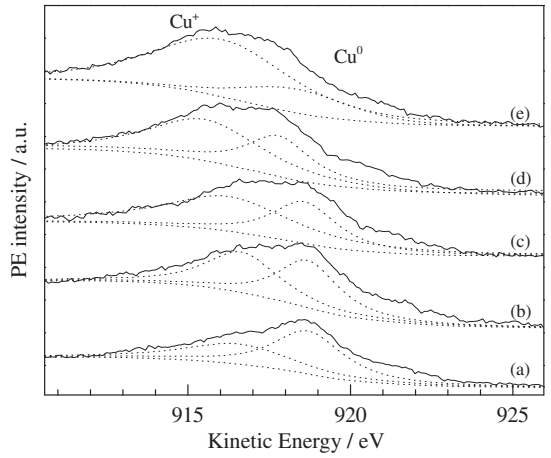

Fig. 7. Cu LMM XAES spectra of Cu–SiO_2 and B–Cu–SiO_2 catalysts after DMO hydrogenation for 6 h: (a) Cu–SiO_2, (b) 0.5B–Cu–SiO_2, (c) 1B–Cu–SiO_2, (d) 3B–Cu–SiO_2, (e) 5B–Cu–SiO_2.

observed in as-reduced and working samples (Figs. S6 and S5). The absence of XPS peaks at 934.9 or 933.5 eV strongly suggested that most cupreous species in +2 oxidation states had been reduced to a low valence state of +1 or 0 after reduction at 623 K. Generally, the binding energy for Cu^0 and Cu^+ species is almost the same, and their difference depends only on the XAES spectra [36]. In the Cu LMM XAES spectra of working catalysts (Fig. 7), asymmetry and broad Auger kinetic energy peaks were observed and deconvoluted into two symmetrical peaks centered at around 916 and 918 eV, corresponding to Cu^0 and Cu^+ species, respectively. The simultaneous existence of Cu^+ and Cu^0 species on silica-supported copper has been extensively discussed [23,37]. From the deconvolution results, boric oxide doping amounts greatly affected the surface Cu^+ and Cu^0 distributions because the molar ratio of surface Cu^+/Cu^0 was gradually enhanced with an increase of the boric loading (Fig. 7 and Table 4; Fig. S6 and Table S2 in the Supplementary Material). The phenomenon is presumed to be induced by a strong interaction between cupreous species and boric oxide, which has a relatively high affinity for electrons. As a result, this leads to a lower degree of reduction of surface copper and a partial positive charge on the copper surfaces.

3.2.5. FTIR study of CO adsorbed on catalysts

To probe the Cu surface, discriminate between metallic copper and cuprous ions, and measure the distribution of different oxidation states of surface copper atoms, FTIR spectroscopy was employed. Fig. 8 shows the IR spectra of CO absorption on as-reduced Cu–SiO_2 and B–Cu–SiO_2 catalysts at room temperature. The as-reduced Cu–SiO_2 catalyst exhibited an asymmetric CO absorption peak at 2090 cm^{-1} and a weak shoulder peak at around 2126 cm^{-1}. The IR band at 2090 cm^{-1} progressively disappeared, whereas the weak band at 2126 cm^{-1} remained during evacuation at room temperature. In contrast, no CO absorption peak was observed on 1B–Cu–SiO_2 at 2090 cm^{-1}, but a strong and symmetric CO absorption peak could be observed at 2126 cm^{-1}. The band at 2126 cm^{-1} did not change significantly under continuous evacuation at room temperature, but it diminished quickly during evacuation at temperatures above 423 K [38,39]. Because no CO absorption peak could be obtained with SiO_2 and B–SiO_2, the CO absorption peaks could be assigned to CO absorption bands on copper species. Assignment of CO absorptions onto Cu^0, Cu^+, and Cu^{2+} surfaces has been well documented in the literature [34,38,40–45]. First, the stretching frequency of CO species absorbed onto cupreous surfaces follows the sequence Cu^{2+}–CO > Cu^+–CO > Cu^0–CO. Second, CO adsorption onto Cu^{2+} and Cu^0 sites is predominantly weak and reversible at room temperature. Third, CO linearly bonded with a surface Cu^+ site has higher thermal stability than Cu^{2+}–CO and Cu^0–CO species. According to these assignments, the CO absorption peaks at 2126 and 2090 cm^{-1} observed on the reduced Cu–SiO_2 and 1B–Cu–SiO_2 catalysts were assigned to Cu^+–CO and Cu^0–CO species, respectively. The IR band near 2090 cm^{-1} assignable to Cu^0–CO suggested that most cupreous species on Cu–SiO_2 had been transformed into metallic Cu after the reduction at 623 K. However, a small amount of partially reduced cupreous species with an

Table 4
Surface Cu component of Cu–SiO_2 and B–Cu–SiO_2 catalysts after DMO hydrogenation for 6 h based on Cu LMM deconvolution.

Catalyst	K.E. (eV)[a]		A.P. (eV)[b]		B.E. of Cu $2p_{3/2}$ (eV)	X_{cu+} (%)[c]
	Cu^+	Cu^0	Cu^+	Cu^0		
5B–Cu–SiO_2	916.1	918.4	1848.8	1851.1	932.7	78.3
3B–Cu–SiO_2	916.4	918.6	1849.1	1851.3	932.7	71.0
1B–Cu–SiO_2	916.3	918.6	1849.0	1851.3	932.7	64.1
0.5B–Cu–SiO_2	916.6	918.7	1849.3	1851.4	932.7	50.5
Cu–SiO_2	916.6	918.7	1849.3	1851.4	932.7	41.4

[a] Kinetic energy.
[b] Auger parameter.
[c] Intensity ratio between Cu^+ and (Cu^+ + Cu^0) by deconvolution of Cu LMM XAES spectra.

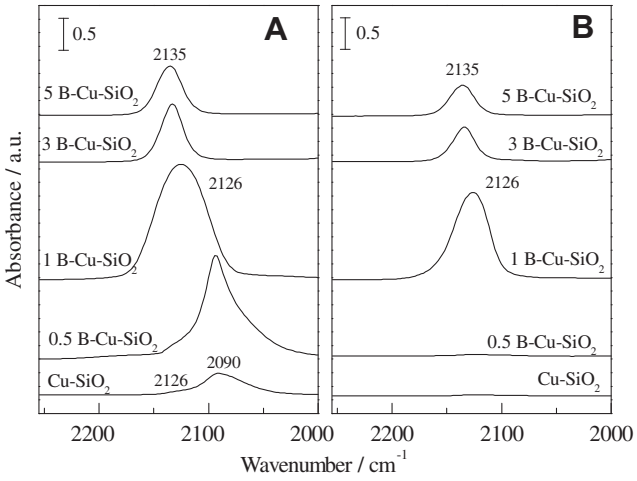

Fig. 8. FTIR spectra of CO absorption on 623-K-reduced Cu–SiO_2 and B–Cu–SiO_2 catalysts after different evacuation times at 298 K: (A) after evacuation for 5 min; (B) after evacuation for 30 min.

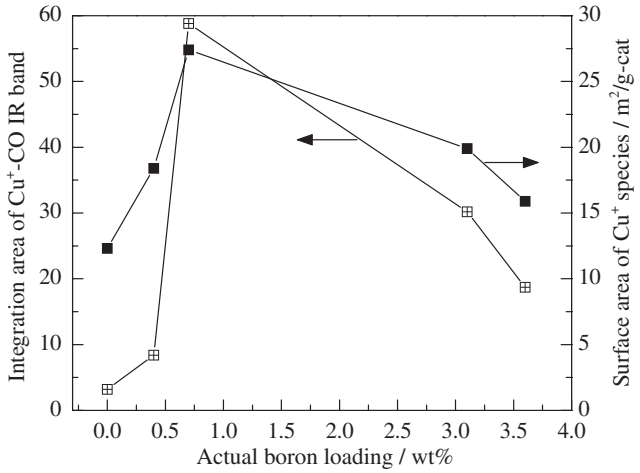

Fig. 9. Variation of integration area of Cu^+–CO IR band and surface area of Cu^+ species on as-reduced Cu–SiO_2 and B–Cu–SiO_2 catalysts as a function of actual boron loading. *Note.* The integration area of the Cu^+–CO IR band was calculated for the IR spectra collected after 30 min of evacuation (Fig. 8), and the surface area of Cu^+ species is estimated with the copper surface values and Cu^0/Cu^+ ratios (Tables 2 and 3, respectively).

oxidation state of +1 was also present on the surface and strongly bound CO molecules with a stable IR peak at 2126 cm^{-1}. On the boric oxide-modified catalyst of B–Cu–SiO_2, the stretching frequency of Cu^+–CO was blue-shifted with an increase of boron oxide concentration. The coexistence of Cu^0 and Cu^+ on the reduced catalyst surface is in accordance with the results of XAES. Similarly, Cu^0 and Cu^+ sites coexisted on the reduced B–Cu–SiO_2 surface, and the molar ratio of Cu^0/Cu^+ varied with the boric oxide doping amount. For 1B–Cu–SiO_2, XAES revealed a surface Cu^0/Cu^+ ratio of 0.56, which was much lower than that for Cu–SiO_2 (1.51). The Cu^+ sites predominating on the copper surface significantly enhanced the intensity of the Cu^+–CO IR band near 2126 cm^{-1} (Fig. 8). Although XAES indicated that the surface Cu^+ species became more dominant when the boric oxide doping amount increased in the range of 110 wt% boron, the accessible surface copper atoms on B–Cu–SiO_2, as determined by N_2O chemisorption, declined because of high boric oxide coverage. Hence, further increasing boric oxide doping amount did not raise, but rather lowered, the intensity of the Cu^+–CO IR band (Fig. 8). Variations of the areas under the Cu^+–CO IR band and surface areas of Cu^+ species on reduced Cu–SiO_2 and B–Cu–SiO_2 catalysts as a function of actual boron loading are shown in Fig. 9. Clearly, the surface areas of Cu^+ species deduced from N_2O chemisorption and XAES reached its highest value with 1B–Cu–SiO_2 having an actual boron loading of 0.7 wt%, and the strongly absorbed CO species on the corresponding catalyst possessed the strongest IR peak at 2126 cm^{-1}.

4. Discussion

Although copper-based catalysts for hydrogenation or hydrogenolysis were extensively studied and various promoters such as chromium, zinc, iron, nickel, magnesium and cobalt have been adopted to modify their catalytic performance [8,23,27,28,40,46], reports related to the effect of boric oxide doping on silica-supported copper remain limited. The essence of the promotion effect for many promoters on copper-based catalysts is still uncertain and in controversy. As to zinc oxide-promoted copper catalysts, some researchers suggested that the electron density of copper tended to increase as a result of oxygen anion vacancies on zinc oxide [47], but the function of zinc oxide in reducing the size of copper crystallites and activation, storage, or spillover of hydrogen were emphasized in other literature [48]. In this study, the Cu–SiO_2 catalysts prepared by urea-assisted gelation were postimpregnated with a suitable quantity of boric oxide, and the as-obtained catalysts exhibited significantly enhanced stability compared with the boric oxide-free ones. The apparent variations in Cu–SiO_2 induced by boric oxide doping were found to be dependent on reducibility, copper dispersion, acidity–alkalinity, and distribution of cupreous species in different oxidation states, essentially inducing structurally related changes in catalytic activity and stability. Among all catalysts tested, 1B–Cu–SiO_2 containing an actual boron concentration of 0.7 wt% displayed the best catalytic performance and stability. Notably, the highest copper dispersion and the greatest amount of surface Cu^+ species were also observed in 1B–Cu–SiO_2, as determined by N_2O chemisorption, XAES, and CO adsorption by IR, implying the importance of high copper dispersion, small copper particles, and surface Cu^+ sites for the catalytic hydrogenation of DMO to EG. In relation to the catalytic functions of Cu^0 and Cu^+ sites in ester hydrogenation, reasonable interpretations suggest that Cu^0 sites dissociatively absorb hydrogen molecules and that Cu^+ sites strongly bind and activate the ester and acyl groups [49]. Accordingly, the efficiency of DMO hydrogenation to EG greatly relies on the synergistic cooperation of Cu^0 and Cu^+ sites present on the catalyst surface and certain kinds of structures of active centers with optimized Cu^0/Cu^+ distributions may exist to achieve a high activity. Boric oxides doped around the cupreous species were expected to be capable of increasing the amount of copper species with partial positive charges because the acidity and electron affinity of boric oxide are greater than that of SiO_2. However, excessively high boric oxide loading inevitably leads to effects of coverage and blocking by B_2O_3. As a result, a decline of exposed and accessible copper surface adversely affects catalytic activity.

Long-term catalytic stability is a necessary feature for industrial catalysts of DMO hydrogenation to EG. The poor lifespan of silica-supported copper catalysts is well known, and synthesis of highly stable copper catalysts loaded onto silica supports remains a significant challenge. A study of the stabilizing effect of boron on Ni catalysts for steam methane reforming proposed that boron tended to selectively block step and subsurface octahedral sites and then reduced the nucleation of graphene islands from steps, prevented coke formation on surfaces, and enhanced the stability of Ni catalysts [26]. However, coking is not the main reason for the irreversible deactivation of copper-based catalysts for oxalate hydrogenation and some changes in the structure and state of catalysts leading to the loss of active sites are considered as important issues. In general, the deactivation of supported copper catalysts was attributed to the coagulation of copper particles, decline in copper dispersion, and change of copper's chemical state [23]. As revealed by XRD measurement for the Cu–SiO_2 catalyst before and after the heat treatment at 623 K (Figs. S2 and S3), the average copper particle size on the partially deactivated catalyst had increased to 12.5 nm, whereas that for the freshly reduced catalyst was only 4.3 nm. However, the copper particle size for the 1B–Cu–SiO_2 catalyst increased only from 4.0 to 7.3 nm. The long-term catalytic evaluation and heat treatment clearly confirmed that the stability of 1B–Cu–SiO_2 was significantly higher than that of boron-free Cu–SiO_2 under identified conditions. These experimental results strongly support the viewpoint that the copper coagulation is one of the essential reasons for the catalyst deactivation. Conventionally, metal sintering is regarded as more likely to happen for low-melting-point metals, such as gold and copper, and the transmigration and aggregation of small metallic particles on the nanoscale may occur at temperatures significantly lower than the melting point. However, thermal stability at the reaction temperature is apparently not the predominant factor that determined the rate of copper particle transmigration and crystallite growth

during DMO hydrogenation to EG because copper particle size increased to 12.4 nm on Cu–SiO_2 after heat treatment at 623 K (Fig. 2), whereas copper particles on Cu–SiO_2 exposed to hydrogen at a significantly higher temperature of 1073 K remained at a small size of 6.3 nm (Fig. S3). Therefore, certain kinds of driving forces other than the simple thermal mass migration induced by DMO hydrogenation possibly accelerated copper coagulation.

From comparison of the XRD patterns of Cu–SiO_2 before and after heat treatment, the Cu_2O phase that emerged on the catalyst after heat treatment was unobservable on the hydrogen-reduced catalyst (Figs. S2 and S3), suggesting that the copper valence transition may have occurred during DMO hydrogenation.

This is supported by other evidence. First, an induction period for reaching the best catalytic performance was repeatedly observed and the length of the induction period often varied with the prereduction program. Usually the catalytic behavior was not very stable at the beginning of the reaction and it took 23 h (sometimes 56 h) to attain a steady state. The presence of this induction period probably indicated that there must be some delicate changes in catalyst structure when the catalyst is exposed to DMO hydrogenation. Second, gray powders of C_2CuO_4 were observed on top of the deactivated catalyst bed. Accordingly, we propose that (1) under the hydrogenation reaction conditions, metallic copper particles, especially nanoparticles, could be oxidized to a state of +1 (the oxidation state +2 could also be occasionally reached) by oxidative substrates, including DMO and MG, among others; (2) hydrogen or active hydrogen species activated by Cu^0 sites tend to bind or spill over to Cu^+ species present on the surface, and then the species are reduced back to Cu^0; (3) this oscillation of the copper chemical state runs through the course of the DMO catalytic hydrogenation. For highly dispersed Cu–SiO_2, the interaction between copper and the silica support is believed to play an important role in stabilizing small copper particles, whereas the frequent transition of copper valence and crystallite phase probably weakened and destroyed this interaction, and finally induced the accelerated aggregation and coagulation of copper particles.

Interestingly, boric oxide doping first inhibited and then accelerated the coagulation of copper particles as doping amount increased, and the optimized doping amount for the best stability was observed for 1B–Cu–SiO_2 with a moderate boron loading of 1 wt% (actual loading 0.7 wt%). The most intense Cu_2O crystallite XRD peaks were also observed on 1B–Cu–SiO_2 after heat treatment at 623 K, probably suggesting that decreasing the reducibility of surface Cu^+ and retaining surface cupreous species in Cu_2O are helpful in promoting catalytic stability. A possible interpretation could be that doping a suitable amount of acidic boric oxide onto the copper surface may decrease the frequency of the copper valence transition by restraining the reducibility of surface Cu^+ species and then significantly retarding the growth of copper particles. This is because the weakening of the interaction between copper and silica support induced by frequent valence transitions of surface cupreous species in DMO hydrogenation circumstance may greatly accelerate the aggregation of copper nanoparticles. On the basis of the above discussion, excessive boric oxide doping is also harmful for stabilizing copper species because once the interaction between cupreous species and SiO_2 is excessively inhibited or substituted by the interaction between cupreous species and boric oxide, transmigration of metallic copper particles tends to speed up in boric oxide with a low melting point and they quickly grow into bulk copper.

5. Conclusions

Suitable boric oxide doping onto Cu–SiO_2 catalysts was found to be an efficient method of improving catalytic stability, as well as EG selectivity, for vapor-phase hydrogenation of DMO to EG. The optimized Cu/B molar ratio was approximately 6.6. With boric oxide properly doped onto the catalyst surface, copper dispersion increased. As demonstrated by N_2O chemisorption and XRD measurement, the growth of copper nanoparticle size was inhibited significantly during DMO hydrogenation. On working catalysts of Cu–SiO_2 and B–Cu–SiO_2, characterizations by XPS, XAES, and *in situ* FTIR of chemisorbed CO revealed that surface Cu^+ species became increasingly predominant as the boric oxide doping amount increased, but the highest quantity of Cu^+ species on the surface was observed for 1B–Cu–SiO_2, because excessively high boric oxide coverage tended to reduce the amount of accessible surface copper atoms. An appropriate distribution of surface Cu^+ and Cu^0 species was presumed to be a key prerequisite for obtaining outstanding hydrogenation performance. Catalyst deactivation was mainly attributed to the decline of Cu dispersion and to the destruction of suitable surface Cu^+ and Cu^0 distribution induced by copper aggregation and coagulation. The strong interaction between acidic boric oxide and surface cupreous species is possibly propitious in minimizing the reducibility of Cu^+ species, maintaining a balance of appropriate Cu^0 and Cu^+ distribution and retarding the surface transmigration of copper nanoparticles, which are essential in gaining excellent catalytic activity and stability.

Acknowledgments

We gratefully acknowledge financial support from the National Natural Science Foundation of China (Nos. 20873108 and 20923004), the National Basic Research Program of China (No. 2011CBA00508), and a Key Scientific Project of Fujian Province (No. 2009HZ0002-1).

Appendix A. Supplementary material

Supplementary data associated with this article can be found, in the online version, at doi:10.1016/j.jcat.2010.10.010.

References

[1] Y.C. Li, S.R. Yan, W.M. Yang, Z.K. Xie, Q.L. Chen, B. Yue, H.Y. He, J. Mol. Catal. A Chem. 226 (2005) 285.
[2] G.H. Xu, Y.C. Li, Z.H. Li, H.J. Wang, Ind. Eng. Chem. Res. 34 (1995) 2371.
[3] J.M. Hollis, F.J. Lovas, P.R. Jewell, L.H. Coudert, Astrophys. J. 571 (2002) L59.
[4] H. Miyazaki, T. Uda, K. Hirai, Y. Nakamura, H. Ikezawa, T. Tsuchie, US 4585890, 1986.
[5] G.S. Chen, B. Xue, H.M. Yan, Chin. J. Catal. 13 (1992) 291.
[6] X.G. Zhao, X.L. Lv, H.G. Zhao, Y.Q. Zhu, W.D. Xiao, Chin. J. Catal. 27 (2004) 125.
[7] W.J. Bartley, W.V. Charleston, US 4677234, 1987.
[8] D.S. Brands, E.K. Poels, A. Bliek, Appl. Catal. A Gen. 184 (1999) 279.
[9] H. Kobayashi, N. Takesawa, C. Minochi, J. Catal. 69 (1981) 487.
[10] T. Sodesawa, M. Nagacho, A. Onodera, F. Nozaki, J. Catal. 102 (1986) 460.
[11] L.R. Zehner, R.W. Lenton, US 4112245, 1978.
[12] P. Fedor, EP 0060787, 1982.
[13] T. Susumu, F. Kozo, N. Keigo, M. Masaoki, M. Katsuhiko, EP 0046983, 1982.
[14] M. Haruhiko, H. Kouichi, U. Taizou, N. Yasuo, I. Seizou, T. Takanori, JP 57123127, 1982.
[15] D.M. Huang, Z.M. Chen, F.X. Chen, P. Lin, H.S. Lan, Y.F. He, Chin. Ind. Catal. 4 (1996) 24.
[16] M. Haruhiko, H. Kouichi, U. Taizou, N. Yasuo, I. Seizou, T. Takanori, JP 57122938, 1982.
[17] M. Haruhiko, H. Kouichi, U. Taizou, N. Yasuo, I. Seizou, T. Takanori, JP 57122939, 1982.
[18] M. Haruhiko, H. Kouichi, U. Taizou, N. Yasuo, I. Seizou, T. Takanori, JP 57122941, 1982.
[19] M. Haruhiko, H. Kouichi, U. Taizou, N. Yasuo, I. Seizou, T. Takanori, JP 57122946, 1982.
[20] H. Kouichi, U. Taizou, N. Yasuo, US 4614728, 1986.
[21] J. Zheng, W.C. Zhu, C.X. Ma, M.J. Jia, Z.L. Wang, Y.H. Hou, W.X. Zhang, Pol. J. Chem. 83 (2009) 1379.
[22] A.Y. Yin, X.Y. Guo, W.L. Dai, K.N. Fan, J. Phys. Chem. C 113 (2009) 11003.
[23] R.G. Wall, Pinole, Calif, US 4149021, 1978.
[24] A.Y. Yin, X.Y. Guo, W.L. Dai, H.X. Li, K.N. Fan, Appl. Catal. A Gen. 349 (2008) 91.
[25] X.Y. Guo, A.Y. Yin, W.L. Dai, K.N. Fan, Catal. Lett. 132 (2009) 22.
[26] J. Xu, L.W. Chen, K.F. Tan, A. Borgna, M. Saeys, J. Catal. 261 (2009) 158.

[27] C.J.G. Van Der Grift, P.A. Elberse, A. Mulder, J.W. Geus, Appl. Catal. A Gen. 59 (1990) 275.
[28] C.J.G. Van Der Grift, A.F.H. Wielers, B.P.J. Jogh, J. Van Beunum, M. De Boer, M. Versluijs-Helder, J.W. Geus, J. Catal. 131 (1991) 178.
[29] C. Carlini, M.D. Girolamo, A. Macinai, J. Mol. Catal. A Chem. 200 (2003) 137.
[30] P.B. Guan, The Manufacture and Application of Fatty Alcohols, Beijing Light Industry Press, Beijing, 1990. pp. 226–228.
[31] Y.Y. Zhu, S.R. Wang, L.J. Zhu, X.L. Ge, X.B. Li, Z.Y. Luo, Catal. Lett. 135 (2010) 275.
[32] K.S.W. Sing, D.H. Everett, R.A.W. Haul, L. Moscou, R.A. Pierotti, J. Rouquerol, T. Siemieniewska, Pure Appl. Chem. 57 (1985) 603.
[33] J. Szanyi, J.H. Kwak, D.H. Kim, S.D. Buiton, C.H.F. Peden, J. Phys. Chem. B 109 (2005) 27.
[34] A. Dandekar, M.A. Vannice, J. Catal. 178 (1998) 621.
[35] L. Chen, Y. Lu, Q. Hong, J. Lin, F.M. Dautzenberg, Appl. Catal. A Gen. 292 (2005) 295.
[36] T. Toupance, M. Kermmarec, J.F. Lambert, C. Louis, J. Phys. Chem. B 106 (2002) 2277.
[37] L.F. Chen, P.J. Guo, M.H. Qiao, S.R. Yan, H.X. Li, W. Shen, H.L. Xu, K.N. Fan, J. Catal. 257 (2008) 172.
[38] I.A. Fisher, A.T. Bell, J. Catal. 178 (1998) 153.
[39] X.H. Mo, J. Gao, J.G. Goodwin Jr., Catal. Today 147 (2009) 139.
[40] G. Busca, J. Mol. Catal. 43 (1987) 225.
[41] A. Davydov, A. Budneva, React. Kinet. Catal. Lett. 25 (1984) 121.
[42] A. Davydov, A. Budneva, D. Sokolovskii, Kinet. Katal. 30 (1989) 1407.
[43] Yu. Lokhov, V. Sadykov, S. Tikhov, V. Popovskii, Kinet. Katal. 26 (1985) 177.
[44] K.I. Choi, M.A. Vannice, J. Catal. 131 (1991) 22.
[45] F. Boccuzzi, A. Chiorino, J. Phys. Chem. B 100 (1996) 3617.
[46] M.C. Engelen, H.T. Teunissen, J.G. Vries, C.J. Elsevier, J. Mol. Catal. A Chem. 206 (2003) 185.
[47] P. Claus, M. Lucas, B. Lücke, Appl. Catal. A Gen. 79 (1991) 1.
[48] F.T. Van de Scheur, L.H. Staal, Appl. Catal. A Gen. 108 (1994) 63.
[49] E.K. Poels, D.S. Brands, Appl. Catal. A Gen. 191 (2000) 83.